



ELSEVIER

Available online at [www.sciencedirect.com](http://www.sciencedirect.com)**ScienceDirect**journal homepage: [www.elsevier.com/locate/he](http://www.elsevier.com/locate/he)

# Comparison of hydrogen transport through pre-deformed synthetic polycrystals and homogeneous samples by finite element analysis



CrossMark

**Yann Charles\***, **Hung Tuan Nguyen<sup>1</sup>**, **Monique Gaspérini**

Université Paris 13, Sorbonne Paris Cité, Laboratoire des Sciences des Procédés et des Matériaux, LSPM, CNRS, UPR 3407, 99 Avenue Jean-Baptiste Clément, F-93430 Villetaneuse, France

---

**ARTICLE INFO**
**Article history:**

Received 19 April 2017

Received in revised form

22 May 2017

Accepted 2 June 2017

Available online 24 June 2017

**Keywords:**

Hydrogen diffusion

Trapping

Crystal plasticity

Finite elements calculations

---

**ABSTRACT**

This study aims at comparing the hydrogen transport in polycrystals and in equivalent homogeneous material, with 3D FE simulations accounting for stress-assisted diffusion and trapping due to plastic strain, in order to examine the hydrogen concentration fields consistency in multi-scale simulations. The effective diffusion features are compared for various sizes of iron polycrystals. For trapping free diffusion, it is shown that hydrogen concentration fields are consistent between scales. When trapping is accounted for, effective diffusion in polycrystals and in homogeneous materials are different, underlying the importance of the trap density function formulation at different scales.

© 2017 Hydrogen Energy Publications LLC. Published by Elsevier Ltd. All rights reserved.

---

## Introduction

Computations of the reliability of metallic structures in hydrogen environment needs to account for material-hydrogen interactions, since hydrogen embrittlement generally first needs hydrogen transport inside the material, as considered in several studies [1,2].

In non-hydride forming single-phase materials, diffusion and trapping at material defects (point defects, grain boundaries, dislocations ...) are the main mechanisms involved in hydrogen transport. Bulk diffusion through interstitial sites is the more common mechanism for hydrogen transport inside the crystal lattice. Short path diffusion along grain boundaries may also contribute to hydrogen transport, especially in fcc

polycrystals [3] with low hydrogen diffusivity. Dislocations also interact with atomic hydrogen and, depending on the conditions and on the material, may lead to antagonist effects on apparent diffusion, which is either slowed by trapping [4], or accelerated by dislocation transport [5,6]. The evolution of dislocations during plastic straining is then expected to modify the hydrogen transport into the material, as observed in several studies [6–8]. From a phenomenological point of view, the hydrogen diffusivity is described by the so-called diffusion coefficient, generally experimentally obtained by electrochemical permeation tests [9,10]. The nature of traps may be investigated by local observations (TEM, ...) and, more often, by global experiments such as positron annihilation [11] and TDS. In these experiments, as the overall response is only available, a strong numerical support is needed to extract the

\* Corresponding author.

E-mail address: [yann.charles@univ-paris13.fr](mailto:yann.charles@univ-paris13.fr) (Y. Charles).

<sup>1</sup> Present Address: Automotive Research & Development (R & D) Center BOSCH Vietnam, E-town 2 Building, 364 Cong Hoa, HCMC, Vietnam.

<http://dx.doi.org/10.1016/j.ijhydene.2017.06.016>

0360-3199/© 2017 Hydrogen Energy Publications LLC. Published by Elsevier Ltd. All rights reserved.

contribution of the trapping and the diffusion phenomenon from cumulative hydrogen curves measurements, using analytical or numerical kinetics models [10,12–15]. Because traps are strongly connected with the microstructural features of materials, reliable prediction of hydrogen diffusivity obviously needs to account for such scales. While homogeneous hydrogen-related simulations are numerous in the literature, few are devoted to polycrystal scales, mainly devoted to the determination of the equivalent hydrogen diffusion coefficient of such an heterogeneous media.

Finite Element (FE) simulation of effective diffusion was conducted by Ref. [16] in duplex stainless steel to highlight the effect of the phase morphology [17]. In polycrystalline aggregates, homogenization and FE simulations have been used to analyze permeation tests. The effect of grain size and sample thickness on the effective diffusion coefficient was analyzed for different virtual microstructures [18,19], based on Fick law using with various diffusion coefficients for bulk, grain boundaries and triple junction in nickel [20]. Elastic crystalline anisotropy and distinction between bulk and grain boundaries diffusion was also used in 2D sequential FE analysis (mechanical then diffusion analysis) to develop a multiscale multiphysics model for HE in polycrystalline nickel [21,22] and to compute the effective diffusivity [23]. Due to the computational cost of the crystals based simulations for initial and boundary values problems of macroscopic samples, a crystal aggregate embedded with homogenized continuum domain is an interesting alternative. Jothi [24] presents a promising coupling of a micro-scale model with the component scale, based on a tie boundary/cut boundary technique, to analyze the multi-scale inter-granular hydrogen embrittlement in a polycrystalline material. In this work, heterogeneous diffusion in microdomains was evidenced while homogeneous behavior is assumed at the larger scale. The hydrogen diffusion coefficient of the homogeneous domain was a theoretical effective value deduced from homogenization for two-phase composites [25]. All these works point out the importance of accounting for heterogeneities at the polycrystal level to describe hydrogen transport, however, FE computations were mainly restricted to 2D models, and the effect of plastic strain on hydrogen transport was not considered.

Plasticity in polycrystals, indeed, is expected to influence the effective diffusivity, due to the heterogeneity of plastic strain and hydrogen dislocation interactions [26]. In literature, few works are focused on the influence of plastic strain on hydrogen transport at the polycrystalline scale, and FE simulations are mainly conducted in 2D. Theses studies focus on the influence of plastic strain field on the hydrogen distribution in grains [27] and on its consequences on the embrittlement process (assuming a FE coupled mechanical-transport scheme [28] or not [29]). To the authors' knowledge, no studies between plastic strain induced-trapping and effective diffusivity at this scale are available.

In this context, the present study aims to focus on the influence of plastic strain-induced trapping on the hydrogen transport in both polycrystalline and homogeneous domains, for comparison purpose. The objective is to analyze the relevant conditions for consistency of hydrogen distribution between the two models, which is a key factor, especially for

submodelling simulations. It is then important to determine the influence of polycrystal features on the transport process, to define a representative elementary volume for trapping influenced hydrogen transport [19].

FE simulations of effective diffusion and hydrogen concentration fields are performed in 3D synthetic polycrystalline aggregates and homogeneous structures, accounting both for stress-assisted diffusion and trapping due to plastic strain. The hydrogen transport equation proposed by Krom [2] is used both for isotropic standard plasticity and for crystalline plasticity. The aim is the comparison, for the same loading, boundary conditions, and finite element features, of the overall diffusion response after plastic prestrain, depending on constitutive mechanical behavior (based on either standard isotropic plasticity or crystal plasticity). To allow such a comparison, the assumptions on material-hydrogen interactions were the same that in Krom work, namely lattice diffusion and trapping by dislocations were considered as the main mechanisms for hydrogen transport in bcc iron. Effect of hydrogen on hardening/softening [30–32], hydrogen enhanced localized plasticity [33–37] and transport by dislocations [6,26,38] were especially not considered.

For the sake of simplicity, only single-phase material is considered here. Pure iron was chosen as a representative bcc material as a first step to access hydrogen embrittlement in ferritic steels, and because of the availability in literature of hydrogen-related parameters [1,2,39,40].

The paper is organized as follows: the constitutive models are first presented, and then, the way they have been implemented in Abaqus FE software. The used geometries and boundary conditions are defined in a second part, as well as the mechanical behavior constitutive laws.

Last, hydrogen diffusion and trapping computations across theses sample are conducted and compared.

## Constitutive models

### Hydrogen diffusion and trapping

Following Krom study [2], the hydrogen concentration  $C$  is assumed to be composed by a diffusive and a trapped part, respectively denoted as  $C_L$  and  $C_T$ , at equilibrium [41] so that (assuming  $\theta_L \ll 1$ ),

$$\frac{\theta_T}{1 - \theta_T} = K_T \theta_L. \quad (1)$$

$K_T$  is here an equilibrium constant with  $K_T = e^{-\frac{W_B}{RT}}$  ( $W_B$  being the trap binding energy), while  $\theta_T$  and  $\theta_L$  denote the trapped and diffusive site occupancy respectively, linked to the corresponding concentration through a trap (resp. diffusion) sites density

$$C_\alpha = N_\alpha \theta_\alpha, \alpha \in \{T, L\}. \quad (2)$$

Thus, inserting relation (2) in (1) formula gives a direct link between  $C_T$  and  $C_L$  [2]

$$C_T = \frac{N_T}{1 + \frac{N_L}{K_T C_L}}. \quad (3)$$

The hydrogen diffusion is assisted by the hydrostatic pressure  $P_H = -\text{tr } \sigma/3$ , and the hydrogen flux is [1,42,43].

$$\varphi = -D_L \nabla C_L - D_L C_L \frac{V_H}{RT} \nabla P_H, \quad (4)$$

where  $D_L$  is the diffusion coefficient,  $V_H$  the partial hydrogen molar volume,  $R$  the Perfect Gas constant and  $T$  the temperature. The global transport equation

$$\frac{\partial C}{\partial t} = \nabla \cdot \varphi \quad (5)$$

leads to the coupled transport equation [2],

$$\frac{C_T(1 - \theta_T) + C_L \frac{\partial C_L}{\partial t} + \nabla \cdot \left( -D_L \nabla C_L - D_L C_L \frac{V_H}{RT} \nabla P_H \right)}{C_L} + \theta_T \frac{dN_T \dot{\bar{\epsilon}}_p}{d\bar{\epsilon}_p} = 0, \quad (6)$$

$N_T$  is here assumed to be only function of the equivalent plastic strain  $\bar{\epsilon}_p$  [44], corresponding to a phenomenological description of the trapping by dislocations.

To solve such a coupled diffusion in Abaqus FE code, several user subroutines are needed [45], as detailed below in Section [Implementations of the coupled transport equation](#), for no standard procedures are so far implemented in commercial programs.

Diffusion and trapping parameters for  $\alpha$ -iron at room temperature are reported on [Table 1](#) [1,2,39].

### Mechanical behavior

Rate-independent elastic-plastic mechanical behavior is considered, using either standard isotropic plasticity or crystal plasticity. Both are expected to give the same overall strain-stress curve provided isotropic texture of the polycrystalline aggregate (and therefore a sufficient high number of grains).

#### Crystal elastoplasticity

The anisotropic elasticity is described by the  $C_{11}$ ,  $C_{12}$  and  $C_{44}$  constants for cubic symmetry (see [Table 2](#)).

$\dot{a}_0$  and  $n$  values were chosen equal to respectively  $0.001 \text{ s}^{-1}$  and 110.

The crystal plasticity is described by a classical viscous formulation [46] for numerical purpose only. The slip rate  $\dot{\gamma}^\alpha$  on a slip system defined by its normal vector  $n^\alpha$  and its slip direction  $m^\alpha$  is related to the resolved shear stress  $\tau^\alpha$  by a power-law relationship:

$$\dot{\gamma}^\alpha = \dot{a}_0 \left( \frac{\tau^\alpha}{\tau_c^\alpha} \right)^n \left| \frac{\tau^\alpha}{\tau_c^\alpha} \right|^{n-1}. \quad (7)$$

$\tau_c^\alpha$  is the critical resolved shear stress,  $\dot{a}_0$  is a reference strain rate, and  $n$  the strain-rate sensitivity, chosen high enough to not induce viscous effects. From slip rates on each system, a global plastic strain rate tensor has been derived

**Table 2 – Elastic parameters for the crystal elastoplastic mechanical behavior [50].**

$C_{11}$ (MPa)	$C_{12}$ (MPa)	$C_{44}$ (MPa)
236900	140600	116000

**Table 3 – Hardening parameters for the crystal elastoplastic mechanical behavior.**

$q$	$h_0$ (MPa)	$\tau_0$ (MPa)	$\tau_s$ (MPa)
1.1	175	30	100

$$\dot{\epsilon}_p = \sum_\alpha (\mathbf{m}^\alpha \otimes \mathbf{n}^\alpha) \dot{\gamma}^\alpha. \quad (8)$$

$\tau^\alpha$  is obtained by

$$\tau^\alpha = \frac{1}{2} (\mathbf{m}^\alpha \otimes \mathbf{n}^\alpha + \mathbf{n}^\alpha \otimes \mathbf{m}^\alpha) : \boldsymbol{\sigma}, \quad (9)$$

where  $\boldsymbol{\sigma}$  is the local stress field;  $\otimes$  denotes the tensorial product, and ‘:’ the tensor contraction. The hardening law is described by Ref. [47]:

$$\dot{\tau}_c^\alpha = \sum_\alpha h_{\alpha\beta} \dot{\gamma}^\beta, \quad (10)$$

$h_{\alpha\alpha}$  represent the self-hardening and  $h_{\alpha\beta, \alpha \neq \beta} = q h_{\alpha\alpha}$  the latent one, with

$$h_{\alpha\alpha} = h_0 \operatorname{sech}^2 \left| \frac{h_0 \gamma}{\tau_s - \tau_0} \right|. \quad (11)$$

where  $\gamma = \sum_\alpha \int_0^t |\dot{\gamma}^\alpha| dt$  is the cumulated shear strain.  $h_0$ ,  $\tau_0$  and  $\tau_s$  are material-dependant parameters. This behavior is implemented in Abaqus through the UMAT developed by Huang [48,49], and modified for the purpose of this study (see [Fig. 1](#)).

The values of  $h_0$ ,  $\tau_0$  and  $\tau_s$  were chosen to be representative of tensile test performed on pure iron single crystals [51,52] (see [Table 3](#)). Only the 12 slip systems {110}{111} for bcc structures were considered in the present study for sake of simplicity. As the plastic strain is only accounted for through the scalar equivalent plastic strain  $\bar{\epsilon}_p$  in Eq. (6), restricting the sets of slip systems contributes also to enhance anisotropy.

#### Isotropic elastoplasticity

Isotropic elasticity is described with Young modulus  $E$  and the Poisson ratio  $\nu$ . The hardening is assumed to obey a Voce law, the yield stress being related to the equivalent von Mises plastic strain by

$$\sigma_Y = \sigma_0 + R_{\text{sat}} (1 - e^{-C\bar{\epsilon}_p}), \quad (12)$$

where  $\sigma_0$ ,  $R_{\text{sat}}$  and  $C$  are material parameters to be identified from the overall response of a polycrystalline aggregate (see [Fig. 1](#)).

**Table 1 – Diffusion parameters for  $\alpha$ -iron.**

$D_L$ ( $\text{m}^2/\text{s}$ ) at $300^\circ \text{ K}$	$V_H$ ( $\text{m}^3/\text{mol}$ )	$\log N_T$	$\text{NL}$ (atom/m3)	$W_B$ (kJ/mol) (dislocations)
$1.27 \times 10^{-8}$	$2 \times 10^{-6}$	$23.26 - 2.33e^{-5.5\bar{\epsilon}_p}$	$8.46 \times 10^{28}$	-60

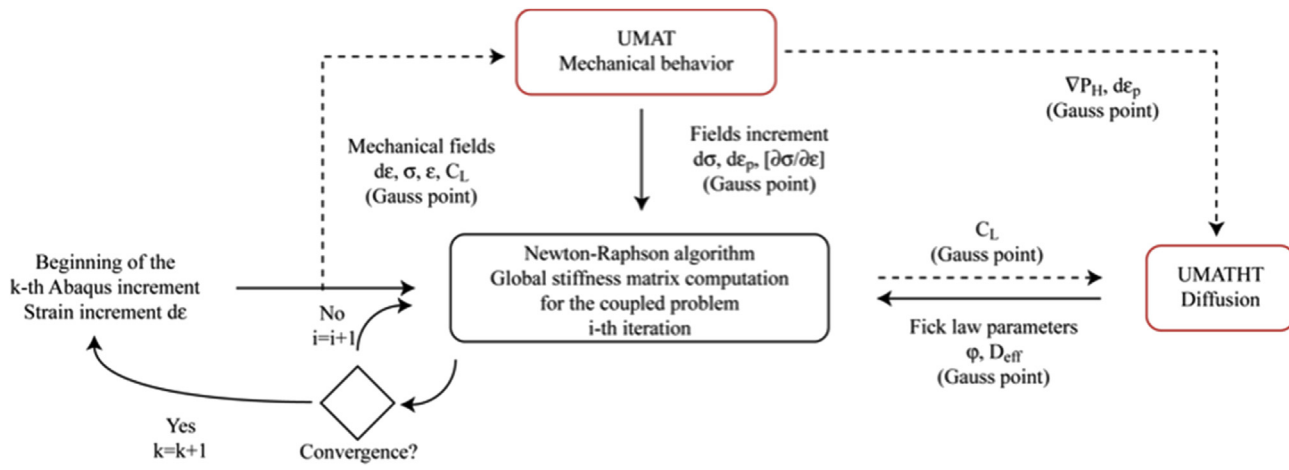


Fig. 1 – Coupled mechanical-diffusion problem implementation in Abaqus.

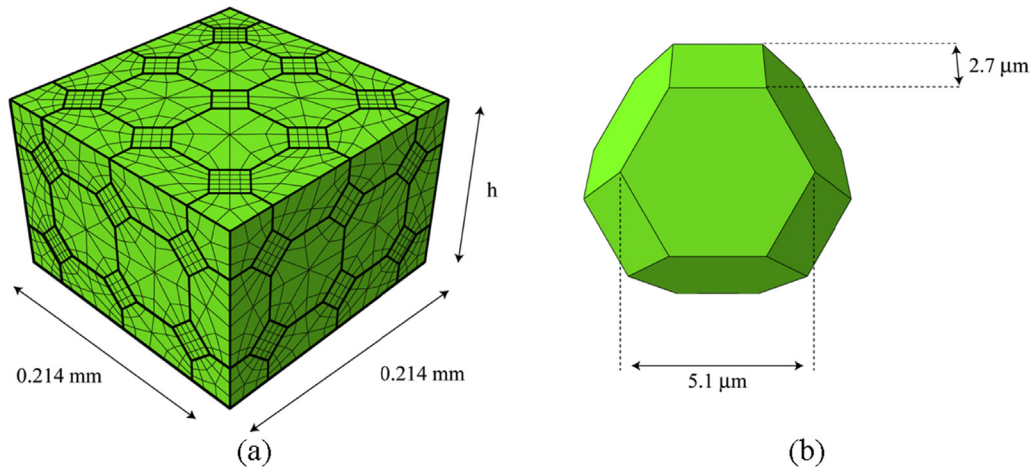


Fig. 2 – (a) Example of a meshed polycrystalline aggregate (66 grains) and (b) illustration of the grain shape.  $h$  denotes the height of the bar.

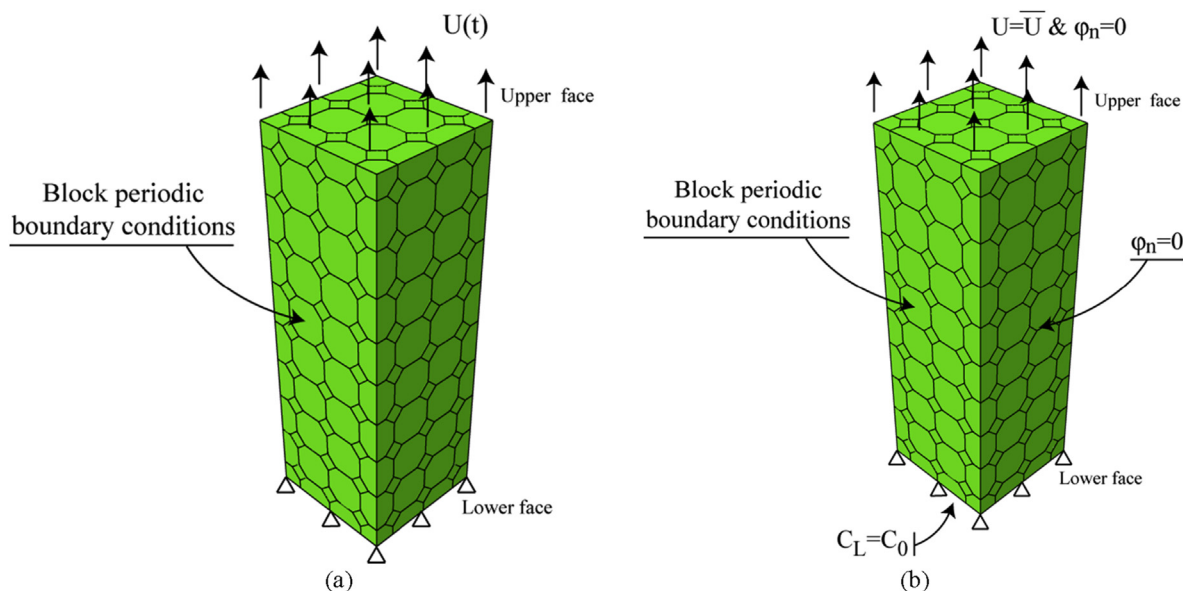


Fig. 3 – Boundary conditions for (a) the mechanical computation up to a macroscopic strain equal to 20% and (b) the diffusion computations considering a fixed applied strain. The bar is here made of 241 grains ( $h = 0.64$  mm).

Section Overall mechanical behavior of the polycrystalline aggregate).

### Implementations of the coupled transport equation

Several implementation strategies of such a coupled behavior in Abaqus can be found in the literature, often using an iterative approach or considering equation as a weak-coupling problem [53,54]. In the present study, the strategy was inspired from Oh work [55]. UMAT and UMATHT subroutines have been developed to respectively compute at each mesh integration point the pressure gradient, the trapped hydrogen concentration, and the modified hydrogen flux [56,57].

Computations are based on the standard Abaqus procedure 'coupled temp-disp', using the thermal degree of freedom -dof- for hydrogen diffusion. The flowchart of this implementation is drawn on Fig. 1.

At the  $i$ -th loop of the Abaqus Newton-Raphson scheme, mechanical fields are computed by the UMAT subroutine, and both the equivalent plastic strain and the hydrostatic pressure gradient are transferred to the UMATHT. These fields are used at the  $i+1$ -th loop to compute the fields linked to the mechanically assisted hydrogen transport equation. When the Newton-Raphson converges towards a solution, both problems are simultaneously solved.

## FE modeling

### Geometry and meshing

The polycrystalline aggregates are designed as parallelepipedic bars with a constant square base with a side length equal to  $\sqrt[3]{0.01} = 0.21544$  mm. The grains are modeled using truncated

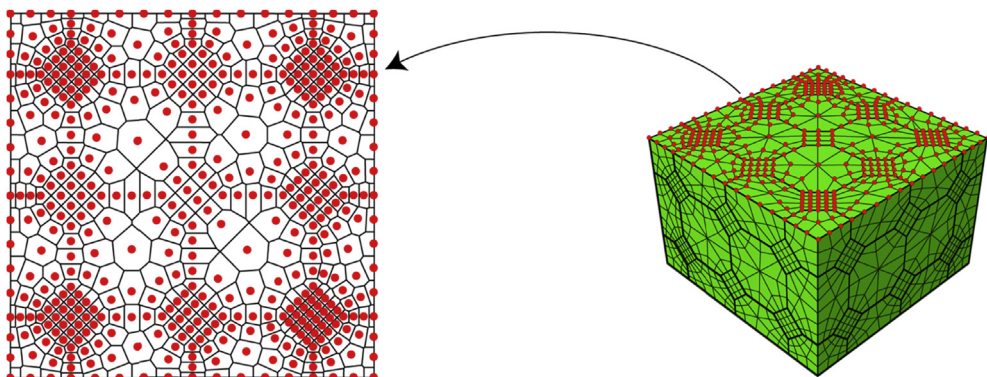


Fig. 4 – Voronoi tessellation of the polycrystal upper face designed for a  $C_L$  repartition statistical treatment; each red seed corresponds to a node (here, 465 nodes). (For interpretation of the references to colour in this figure legend, the reader is referred to the web version of this article.)

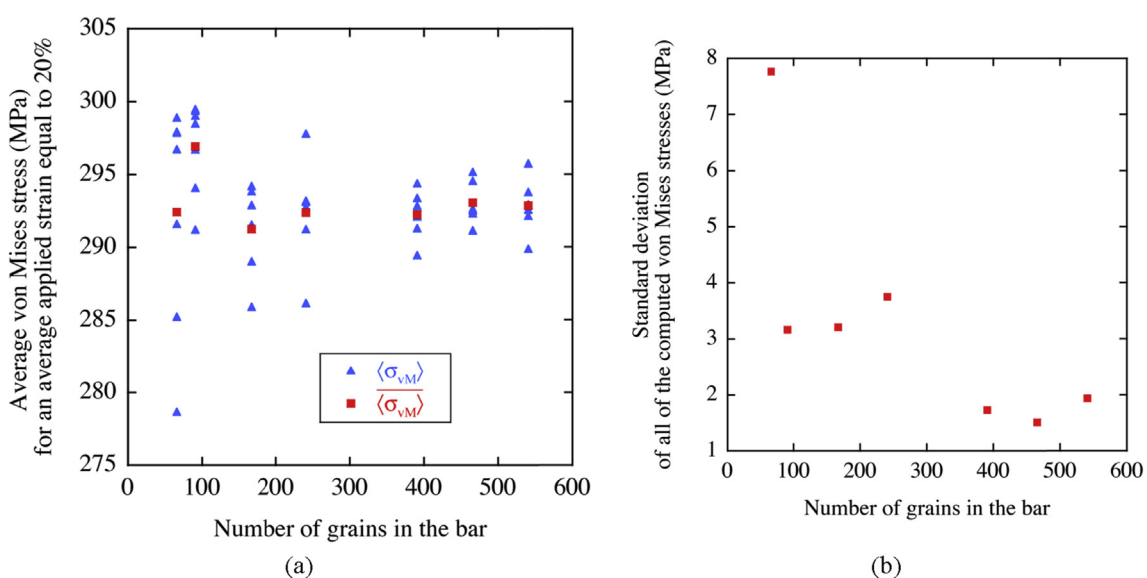
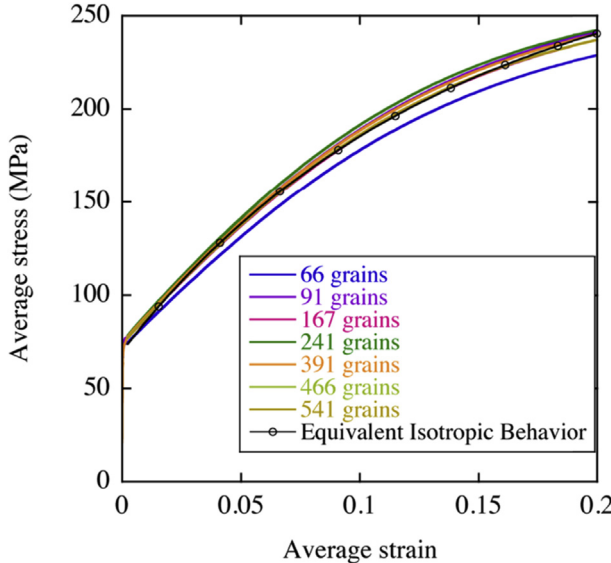


Fig. 5 – (a) Average von Mises stress values (blue dots) for an average applied strain of 20%, for all configurations, and their mean values for each bar configurations (red dots). For every grain number, 6 to 7 computations have been performed. (b) Standard deviation of the average von Mises stress values for each bar configuration. (For interpretation of the references to colour in this figure legend, the reader is referred to the web version of this article.)

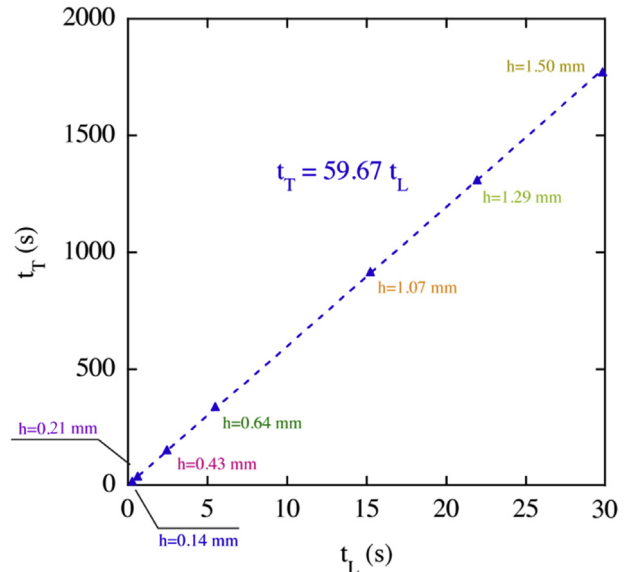
**Table 4 – Mechanical parameters corresponding to the average polycrystal behavior.**

E (GPa)	$\nu$	$\sigma_0$ (MPa)	$R_{\text{sat}}$ (MPa)	C
215	0.3	70.3	220.4	7.4

These parameters define the reference behavior for the coupled transport computations.

**Fig. 6 – Overall  $\langle \epsilon \rangle\langle \sigma \rangle$  curves for the different computations of aggregates, and the identified homogeneous hardening.**

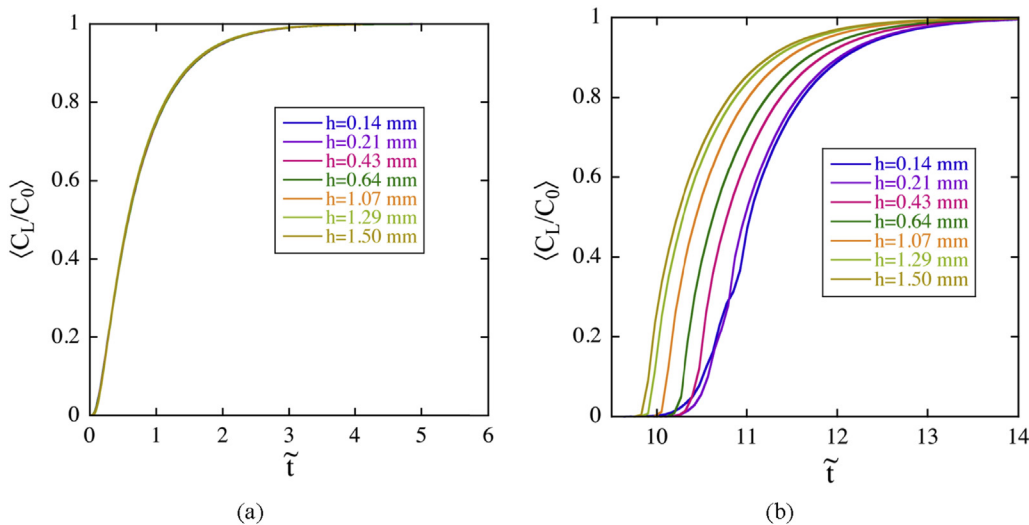
octahedron (see Fig. 2a for 66 grains), with a constant size (see Fig. 2b). Such a regular grain shape allows to insure a perfect morphology reproducibility whatever the bars, and consequently to limit the influence of the grain morphology in the

**Fig. 8 – Diffusive time lag versus trapping-induced one for the homogeneous bars.**

comparison process. The number of grains in the polycrystal is controlled by the bar height  $h$ . Each grain is meshed with 60 full integration tri-linear elements. Different grain numbers are considered in the following: 66, 91, 167, 241, 391, 466 and 541 grains (corresponding to height  $h = 0.14, 0.21, 0.43, 0.64, 1.07, 1.29$  and  $1.50$  mm respectively). It is worth to underline that for a given  $h$  value, the mesh is exactly the same whatever the constitutive law, for the sake of comparison.

All geometries have been generated by the Neper program [58] and imported in Abaqus CAE using python scripts [59].

Last, grain orientations are defined by an ORIENT User Subroutine [45], using random sets of Euler angles  $(\varphi_1, \Phi, \varphi_2)$ , assuming an overall isotropic texture.

**Fig. 7 –  $\langle C_L/C_0 \rangle$  variation at the upper face of the bars considering an isotropic mechanical behavior and (a) without or (b) with trapping.**

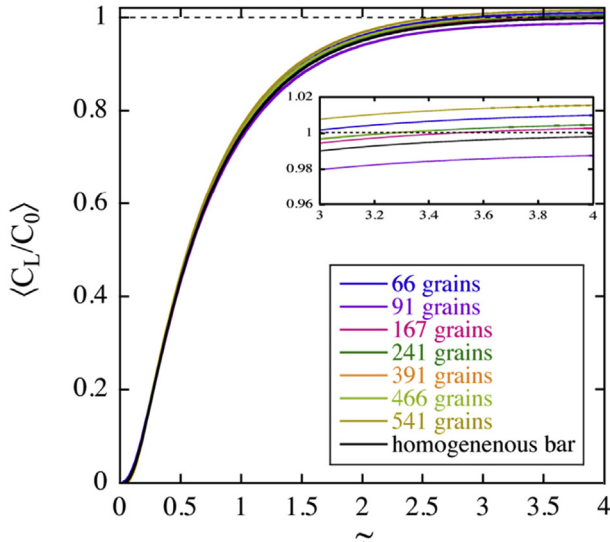
### Boundary conditions

The computation is made of two-steps: first a purely mechanical simulation, secondly a diffusion one under a constant mechanical loading.

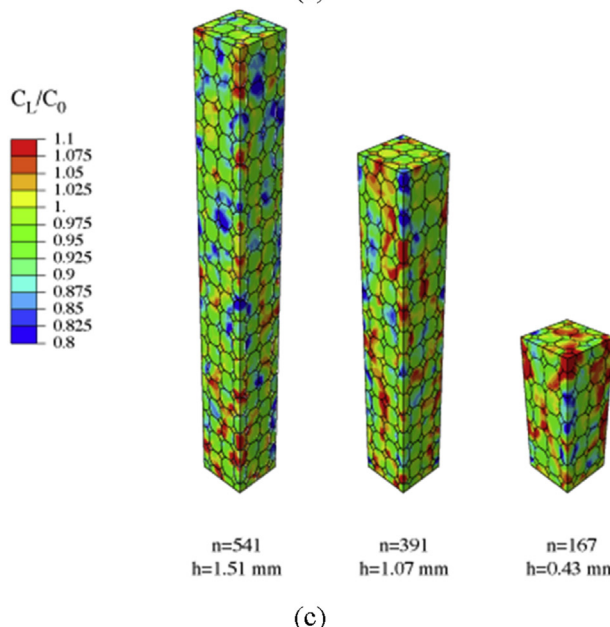
First, a displacement, corresponding to an overall 20% uniaxial strain, has been applied on the upper face of the aggregates, while symmetric boundary conditions have been set on the lower one (Fig. 3a). On the side faces, uniform mixed-

orthogonal (or block) conditions have been defined to model periodicity [60,61].

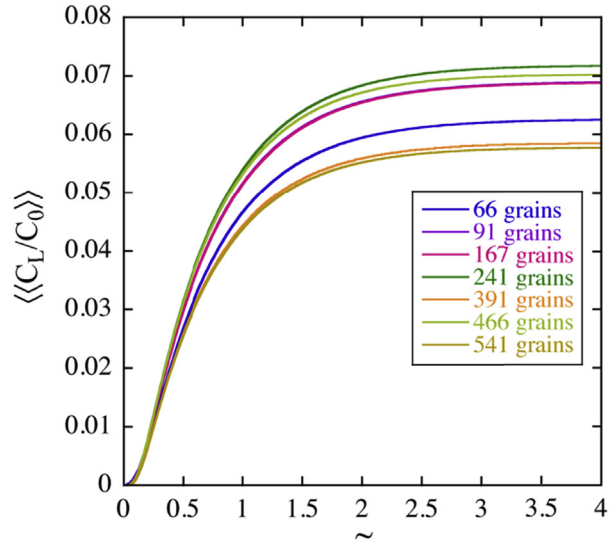
Once the mechanical loading is achieved, hydrogen transport under constant strain is simulated. A zero normal flux is imposed on each polycrystal faces but on the lower one, where  $C_L=C_0$  [1,40] is instantaneously imposed at the beginning of the diffusion step (Fig. 3b). Hydrogen transport and trapping then occur, based on Eq. (6); the computation is stopped as soon as the steady state is detected.



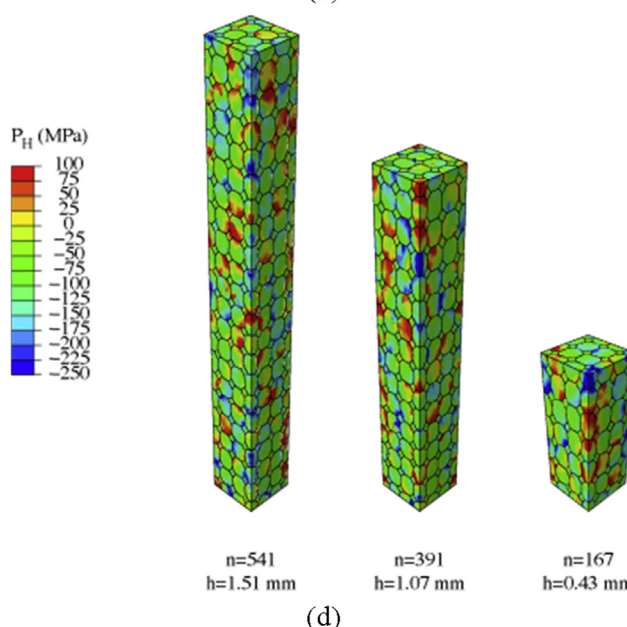
(a)



(c)



(b)



(d)

**Fig. 9 – Influence of the grain number on the (a)  $\langle C_L/C_0 \rangle$  evolution and (b) the related standard deviation on the bars upper faces; the dimensionless diffusive hydrogen concentration density function is also plotted at the end of the diffusion process for 66 (blue), 241 (green) and 541 (brown). (c-d) Hydrogen and hydrostatic pressure repartition at the end of the diffusion process. As expected from Eq. (4), there is a strong correlation between both fields. (For interpretation of the references to colour in this figure legend, the reader is referred to the web version of this article.)**

For all computations, the diffusive hydrogen concentration values  $C_L$  has been saved for each upper face nodes, and at each computed time; the temporal evolution of the upper face  $C_L$  repartition has then been characterized using a statistical treatment. To compute both  $C_L$  average and standard deviation values, the value of each node has been weighted by the surface of the corresponding cell in the Voronoi tessellation of the bar upper face (see Fig. 4).

### Overall mechanical behavior of the polycrystalline aggregate

To compare the influence of the local heterogeneity on the mechanically-assisted hydrogen transport, both homogeneous and polycrystalline samples must give the same overall  $\sigma$ - $\epsilon$  curve. Assuming the local crystalline hardening, the identification of the homogeneous macroscopic one leads to the definition of a Representative Elementary Volume (REV) mechanically statistically representative.

### Identification of the homogeneous hardening

To identify the global hardening behavior of the polycrystal (Eq. (11)), simulation of the mean stress-strain curves of polycrystalline aggregates have been performed. First, the best compromise between the number of grains and elements in 3D aggregates and the computation cost has to be determined, since various REV sizes may be found in the literature. The grain number typically ranges between around 200 [62,63] and 500 [60,64], even if some work points out that as low as 5 grains might be used in case of periodic conditions [65]. Huge variations may be found on the number of integration points, from only one element per grain if the number of grain is high enough [63] to 600 integration points per grain [62].

Due to this lack of consensus, identification of the REV has been performed for the considered polycrystalline bars, deformed in a tensile test up to an average strain  $\langle \epsilon \rangle = 20\%$  (according to Section Boundary conditions); for each bars, from 6 to 7 computations have been made, from which average mechanical fields have been computed by python scripts. On Fig. 5a are shown the values of the average von Mises stress  $\langle \sigma_{vM} \rangle$  for  $\langle \epsilon \rangle = 20\%$  for each computations (blue dots), as well as their mean values  $\overline{\langle \sigma_{vM} \rangle}$  for each grain number (red dots). It can first be observed that  $\overline{\langle \sigma_{vM} \rangle}$  values do not really depends on the grain number (except for 91 grains), evolving between 291 and 293 MPa. Dispersion of  $\langle \sigma_{vM} \rangle$  values, however, decreases while the number of grain increases, and seems stabilized for grains number greater than 300–350, as illustrated by the standard deviation  $\overline{\langle \sigma_{vM} \rangle}$  shown on Fig. 5b. Based on these results, the homogeneous hardening law have been identified using a least square method, assuming the Eq. (12) (see Table 4 and Fig. 6); isotropic elastic parameters E and  $\nu$  have been directly identified from computations:

$$\left\{ \begin{array}{l} E = \frac{\langle \sigma \rangle}{\langle \epsilon \rangle} \\ \nu = -\frac{\langle \epsilon_T \rangle}{\langle \epsilon \rangle} \end{array} \right. \quad (13)$$

where  $\langle \sigma \rangle$  and  $\langle \epsilon \rangle$  represents the average stress and strain in the traction direction, while  $\langle \epsilon_T \rangle$  represents the average strain

on a direction normal to the traction one (having checked that, whatever  $\langle \epsilon \rangle$  values,  $\langle \sigma_T \rangle = 0$  MPa).

## Results

Two sets of computations have been performed.

- a trapping free diffusion, in which the mechanical fields influence on hydrogen transport is only due to the  $P_H$  term in Eq. (4);
- a coupled transport and trapping process, based on Eq. (6).

For these two sets, both isotropic and crystal hardening has been used to get the influence of the polycrystalline nature of the considered volumes on the transport process.

For each height bar value  $h$ , the dimensionless time for diffusion  $\tilde{t} = t D_L / h^2$  has been used [66], and the normalize average diffusive hydrogen  $\langle C_L / C_0 \rangle$  concentration on the bars upper faces have been focused on (see Section Boundary conditions for its computation).

### Reference transport curves in homogeneous bars

On Fig. 7 are reported the transport curves for the isotropic bars, with and without trapping.

As expected, the  $\langle C_L / C_0 \rangle$  curves are size-independent when plotted vs the dimensionless time (Fig. 7a). On the contrary, they depend on  $h$  when trapping is accounted for (Fig. 7b), and it can be observed that the average ('apparent') diffusion coefficient increases with  $h$ : the greater the apparent coefficient, the faster the diffusion though a given distance in term of  $\tilde{t}$ .

To discuss the influence of trapping on hydrogen transport, the time lag method has been used [8], the trap-free time lag  $t_L$  being defined as [67].

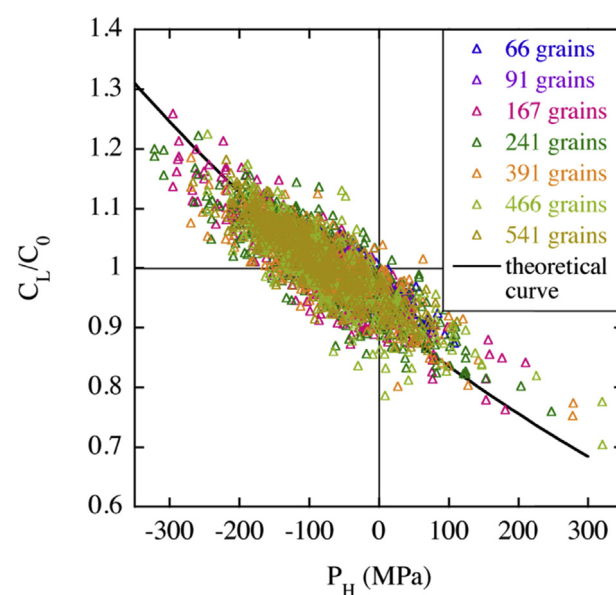


**Fig. 10 – Repartition on the  $C_L$ - $P_H$  points for all upper faces nodes. In both cases, the theoretical curve is defined by Eq. (17), using the value for  $V_H$  defined in Table 1.**

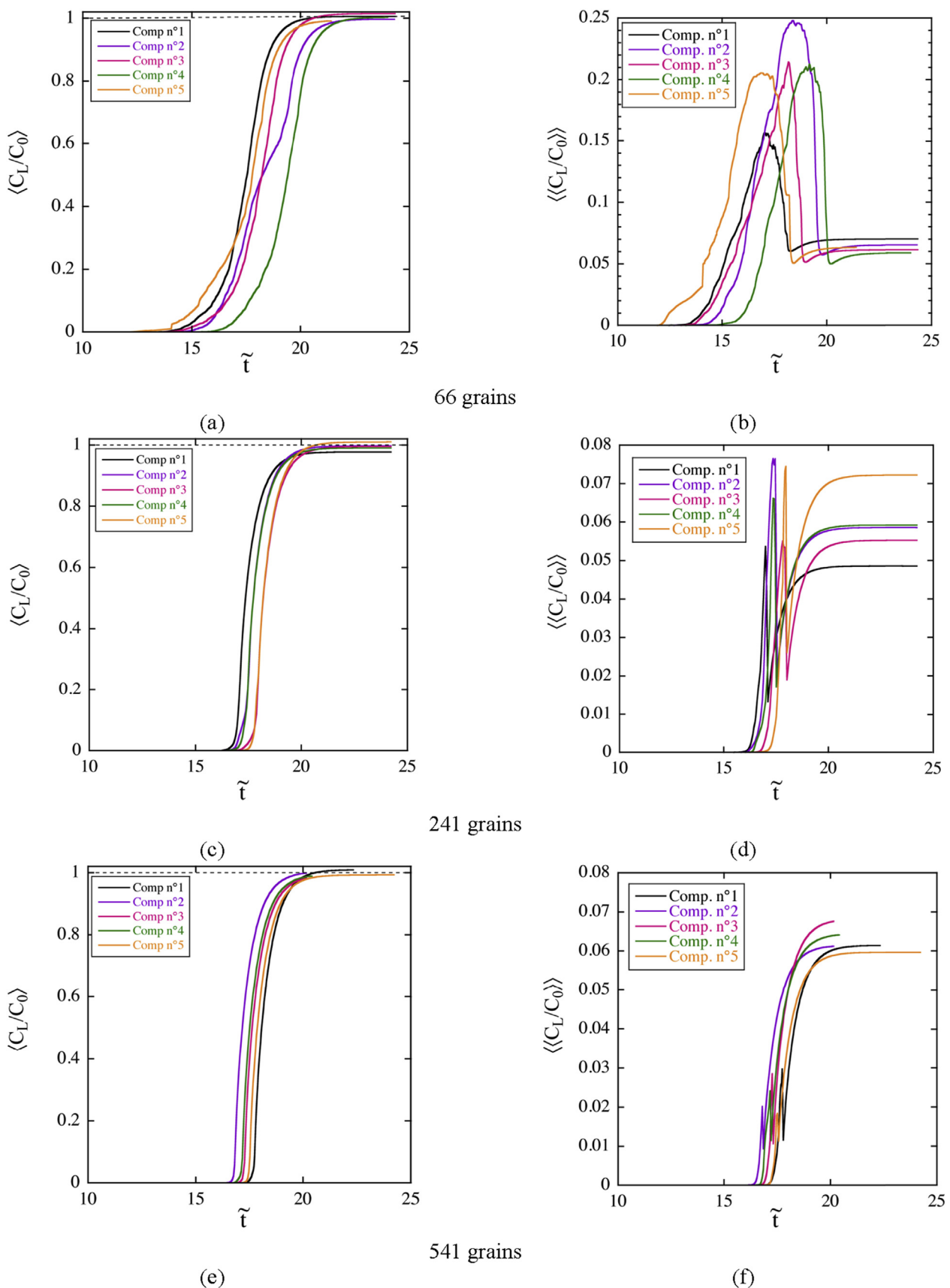


**Fig. 11 – Average normalized diffusive hydrogen concentration and related standard deviation for three bar configurations (a–b: 66 grains; c–d: 241 grains; e–f: 541 grains).**

$$t_L = \frac{h^2}{6D_L}, \quad (14)$$

and the time lag with trapping  $t_T$  being extracted from computations results (Fig. 7b) [66]. These two times lag are supposed to be linked by a linear relationship (for permeation test) by Refs. [44,68].

$$\frac{t_T}{t_L} - 1 = \alpha \frac{N_T}{C_0}, \quad (15)$$

where  $C_0$  represents the boundary condition,  $N_T$  the trap density. Plotting  $t_L$  vs  $t_T$  for the present configuration (Fig. 8), leads to a linear relationship for which  $\alpha = 4$ . It is worth noting that for permeation test configurations (for which steady-state  $C_L$  variation in the sample differs from the studied configuration),  $\alpha = 3$ .

### Trapping-free hydrogen transport in polycrystalline bars

Trapping-free diffusion computations have been performed for all considered bars, using the mechanical behavior described on Section [Crystal elastoplasticity](#), and compared to the isotropic case (Fig. 9a).

As observed, the stress field heterogeneity (and thus the  $P_H$  one) has no influence on the hydrogen transport kinetics along the different polycrystals, since all  $\langle C_L/C_0 \rangle - t$  curves are superposed (Fig. 9a), and comparable to the homogeneous ones (defined from Fig. 7a). From this superposition, it can be stated that the trapping-free hydrogen transport features in an heterogeneous media are the same than the equivalent homogeneous ones; the polycrystal effective diffusion coefficient is consequently  $D_L$ . Such a result agrees with literature [19,24], and insures the consistency of hydrogen concentration fields in multi-scales FE simulations.

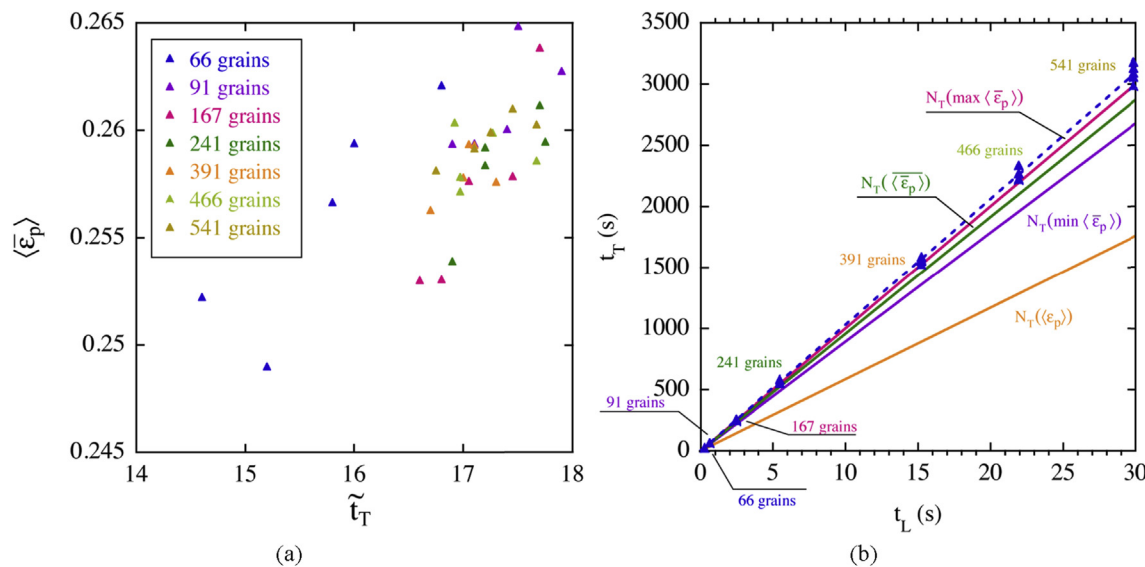


**Fig. 12 – (a) Relationship between the average equivalent plastic strain other the polycrystals and the dimensionless time lag with trapping, and (b) diffusive time lag versus trapping-induced one for the polycrystals. Blue dots denote  $t_L - t_T$  points, and lines the theoretical linear relationship given on Eq. (15), considering, its slope computation  $\alpha = 4$ , and several  $N_T$  values. Dashed blue line is the best linear fit using a least square method.**

The stress field heterogeneity, however, impacts the steady state values of the polycrystalline  $\langle C_L/C_0 \rangle - t$  curves, which are no equal to 1, as it could have been expected. This observation might be linked to the pressure heterogeneity (see Fig. 9c–d for an illustration), and especially the differences between the lower face stress state (where  $C_L=C_0$  is imposed) and the upper face one, as explain in the following.

From Eq. (6), assuming that the steady state has already been reached, and underlying that, in the considered configurations, this leads to a zero hydrogen flux everywhere, it can be written

$$\nabla C_L + C_L \frac{V_H}{RT} \nabla P_H = 0, \quad (16)$$

and thus,

$$C_L = C_0 \exp \left[ -\frac{V_H}{RT} (P_H - \langle P_H \rangle_{inf}) \right], \quad (17)$$

as  $C_L=C_0$  for  $P_H = \langle P_H \rangle_{inf}$ , the mean hydrostatic pressure on the polycrystal lower face (computed with the same method as the one used for the upper faces, see Section [Boundary conditions](#)). On the polycrystal upper faces, computations should consequently exhibit a linear relationship between  $\langle \ln C_L/C_0 \rangle$  and  $\langle P_H \rangle$ , with a slope equal to  $-V_H/RT$  (The used  $V_H$  value is the one reported on Table 1,  $T$  being equal to 293 K).

It can be observed on Fig. 10 that Eq. (17) gives a good tendency for the link between the levels of  $C_L$  and pressure on the polycrystal upper faces. The dispersion of the results might be linked to the one summarized on standard deviation curve evolution (Fig. 9b).

### Trapping and transport of hydrogen in polycrystalline bars

Last, trapping-affected transport process has been conducted in all bars. To look after the heterogeneous mechanical

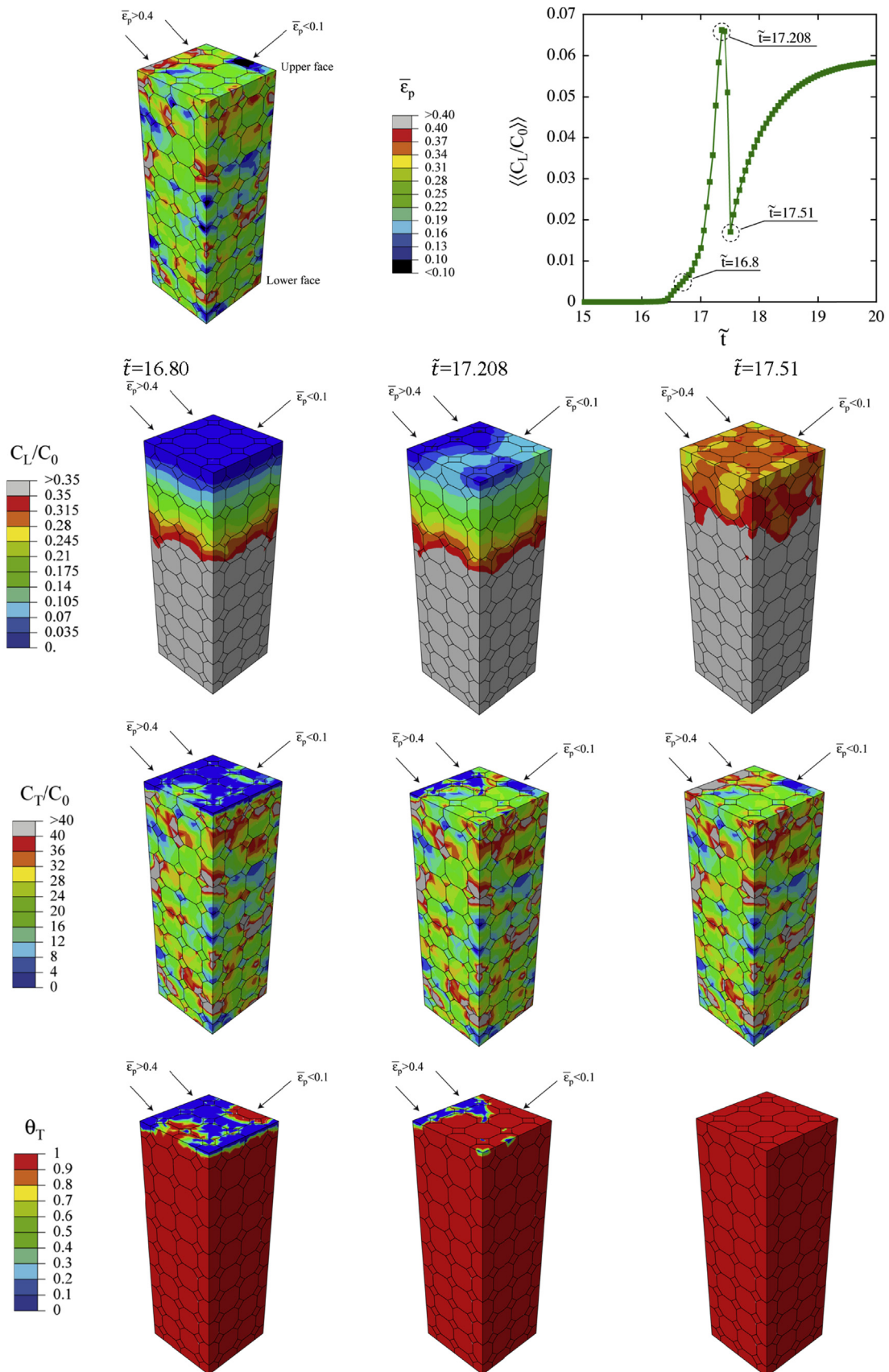


**Fig. 13 –** Equivalent plastic strain repartition in the bar at the end of the mechanical loading, and the  $\langle\langle C_L/C_0 \rangle\rangle - \tilde{t}$  corresponding curve during the transport process. Three times are considered, located on the beginning, at the top and at the end of the peak;  $C_L/C_0$  and  $C_T/C_0$  repartitions, and trapping site occupancy  $\theta_T$  are focused on for these times.

behavior influence on the diffusive hydrogen concentration on the upper face, five computations for each polycrystal configuration have been performed. On Fig. 11 are plotted the results for three of them (66, 241 and 541 grains).

As it can be observed, even for a given bar configuration, the  $\langle C_L/C_0 \rangle - \tilde{t}$  curves are not superposed, inducing a variation of the apparent diffusion coefficient, with a steady state value which are not equal to one, as in the trapping-free configuration (and consequently linked to the stress field heterogeneity). Standard deviations, for the same reasons, tend, at steady state, toward values that are comparable to the trapping-free ones.

Two main features have here to be underline, linked to the plastic strain repartition in the polycrystals.

First,  $\langle C_L/C_0 \rangle - \tilde{t}$  curves are here not superposed for a given polycrystal configuration, due to the variation of the equivalent plastic strain repartition (linked to the average von Mises stress dispersion illustrated on Fig. 5a), and its average value other the whole bar  $\bar{\epsilon}_p$ . It is worth noting that, while all average plastic strains  $\epsilon_p$  in the traction direction are close to 20% (and the transverse ones 0, leading to average Poisson ratios equal to 0.5), the equivalent plastic strain ones  $\bar{\epsilon}_p$  are close to 26%. Such a value is not surprising, due to the plastic strain heterogeneities in the polycrystal (see Fig. 13). On Fig. 12a are plotted, for all polycrystal configurations, the  $\bar{\epsilon}_p - \tilde{t}_T$  points; it can be observed a global increasing tendency: the greater the  $\bar{\epsilon}_p$  value, the greater dimensionless time lag with trapping.

On Fig. 12b are plotted the  $t_L - t_T$  points for all polycrystals; the general appearance of this cloud of dots is a linear one. Reusing Eq. (15), with  $\alpha = 4$ , a theoretical slope can be computed, using either, for the  $N_T$  computation, the average plastic strain in the tensile direction  $\langle \epsilon_p \rangle = 20\%$ , the mean value of the average equivalent plastic strains  $\langle \bar{\epsilon}_p \rangle = 25.8\%$ , the maximum and minimum average equivalent plastic strains values  $\min(\bar{\epsilon}_p) = 24.9\%$  and  $\max(\bar{\epsilon}_p) = 26.5\%$  overs all computed configurations. It can be observed that the best slope is obtained using  $N_T(\max(\bar{\epsilon}_p))$ , even if it remains lower than the one identified by a least square method; this slope is quite twice as the one identified for the homogeneous bars.

The immediate consequence of such a result is that the simple extension at the polycrystal scale of the trap density  $N_T$  as a function of the equivalent plastic strain does not allow to reproduce the macroscopic hydrogen transport kinetics features. Further investigations on trapping due to plastic slip at the local scale, and to the underlying hydrogen-dislocations interactions are consequently needed, to account for local trapping heterogeneities, and to extract a more relevant way to express the  $N_T$  function.

Second,  $\langle \langle C_L/C_0 \rangle \rangle - \tilde{t}$  curves exhibit a peak during the transient stage, which height decreases while the number of grains increases. This peak is linked to the plastic strain heterogeneity of the upper face, which leads to very different diffusion characteristics of the upper grains, as illustrated on Fig. 13 for 241 grains and the 4th computation (see Fig. 11d). For this latter configurations, three times are considered, located at the beginning, at the top and at the end of the peak. Both diffusive hydrogen concentration and trap site occupancy repartition in the bar are then drawn.

From the equivalent plastic strain repartition, it can first be observed that, on the bar upper face, one grain has a very low

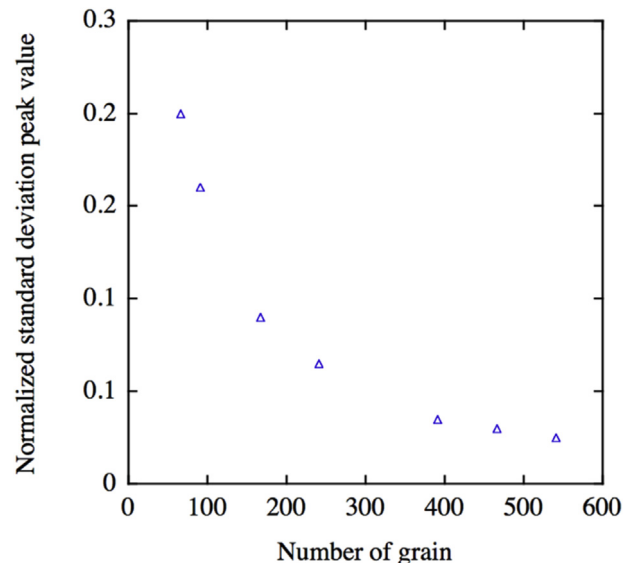


**Fig. 14 – Evolution of the normalized standard deviation peak with the number of grains in the bars.**

plastic strain ( $<0.1\%$ ), i.e. a low trapping site density value, and several have a high one ( $>0.4\%$ ). This leads to a very heterogeneous transport process, as illustrated by the  $\theta_T$  maps.

At the very beginning of the peak, the hydrogen concentration on the upper face is very low ( $<0.05C_0$ ), while the traps are filled only on the grains experiencing the lower plastic strain. As transport occurs, traps are gradually filled, from the less deformed grains to the most ones, reaching a  $C_L$  value close to  $0.1C_0$ , but for the grains with the higher plastic strain, where  $C_L$  remains as low as at the beginning of the peak. This point corresponds to the most important dispersion in term of  $C_L$  values. Hydrogen transport eventually occurs through highly deformed grains, filling all remaining traps, decreasing the  $C_L$  dispersion on the upper face: at the end of the peak, the  $\langle \langle C_L/C_0 \rangle \rangle - \tilde{t}$  curve evolution look alike the trapping free one, corresponding to a transport process mainly affected by the stress field heterogeneity.

On Fig. 14 are plotted the average peak height versus the number of grains in the polycrystal: such an evolution denotes the trends of the  $C_L$  statistical repartition characteristics on the polycrystal upper faces to converge towards the trapping-free ones, as the number of grains increases. In other words, when the grain number in the polycrystal increases, equivalent plastic strain dispersion influence on the transport process tends to decrease, defining a Representative Elementary Volume for the trapping and transport process.

The trapping and transport REV minimum grains number might be set as 300, according to Fig. 14, i.e, the same one as the mechanical REV (Section Identification of the homogeneous hardening).

## Conclusions

This study aimed at comparing the hydrogen transport in polycrystals and in equivalent homogeneous domain, by

performing 3D FE simulations and accounting for stress-assisted diffusion and trapping due to plastic strain. For various sizes of polycrystals and related homogenous domain, the effective diffusion features have been compared.

For a trapping-free transport, computations have shown that there were no differences between diffusion in polycrystalline or in equivalent homogeneous material. As a consequence, consistency is then assured for computations based on submodelling or with a polycrystal embedded in an homogenous domain.

While accounting for plastic strain induced trapping, however, important differences have been exhibited between polycrystalline and homogeneous bars. Hydrogen transport in polycrystals has been found about twice slower than transport in equivalent homogeneous materials. The scale transition is consequently not obvious, and particular precautions are needed to get a hydrogen concentration field consistency at the boundary of the polycrystal and the homogeneous media. For the sake of simplicity, in the present study, the macroscopic formulation for the trap density  $N_T$  has been transposed at the crystal scale, using the equivalent plastic strain as in literature. From the obtained results, it appears, however, that this assumption does not allow to fully accounting for the local plastic strain heterogeneity, and thus, trapping at the crystal scale.

Further experimental works are needed to fully characterize the influence of dislocations induced trapping on hydrogen transport at that scale, in order to better model the diffusion process in polycrystals. In particular, accounting for localized plasticity (HELP mechanism) and hydrogen effect on hardening behavior may improve the simulations. To more precisely analyze size effects, more realistic microstructures have to be considered, because of the influence of morphology on diffusion [17], and the use of the promising strain gradient plasticity approach [69–72] could help to better describe the localized plastic strains at single crystal scale.

## REFRENCES

- [1] Sofronis P, McMeeking RM. Numerical analysis of hydrogen transport near a blunting crack tip. *J Mech Phys Solids* 1989;37:317–50. [http://dx.doi.org/10.1016/0022-5096\(89\)90002-1](http://dx.doi.org/10.1016/0022-5096(89)90002-1).
- [2] Krom AHM, Koers RWJ, Bakker AD. Hydrogen transport near a blunting crack tip. *J Mech Phys Solids* 1999;47:971–92. [http://dx.doi.org/10.1016/S0022-5096\(98\)00064-7](http://dx.doi.org/10.1016/S0022-5096(98)00064-7).
- [3] Oudriss A, Creus J, Bouhattate J, Savall C, Peraudeau B, Feaugas X. The diffusion and trapping of hydrogen along the grain boundaries in polycrystalline nickel. *Scr Mater* 2012;66:37–40. <http://dx.doi.org/10.1016/j.scriptamat.2011.09.036>.
- [4] Lee J-L, Lee J-Y. The effect of lattice defects induced by cathodic hydrogen charging on the apparent diffusivity of hydrogen in pure iron. *J Mater Sci* 1987;22:3939–48. <http://dx.doi.org/10.1007/BF01133343>.
- [5] Hirth JP, Johnson HH. On the transport of hydrogen by dislocations. *Atomistics of fracture*. Boston, MA: Springer US; 1983. p. 771–87. [http://dx.doi.org/10.1007/978-1-4613-3500-9\\_26](http://dx.doi.org/10.1007/978-1-4613-3500-9_26).
- [6] Hwang C, Bernstein IM. Dislocation transport of hydrogen in iron single crystals. *Acta Metall* 1986;34:1001–10. [http://dx.doi.org/10.1016/0001-6160\(86\)90209-9](http://dx.doi.org/10.1016/0001-6160(86)90209-9).
- [7] Donovan JA. Accelerated evolution of hydrogen from metals during plastic deformation. *Metall Trans A* 1976;7:1677–83. <http://dx.doi.org/10.1007/BF02817885>.
- [8] Hwang C, Bernstein IM. The fundamentals of dislocation transport of hydrogen in BCC iron. 1984.
- [9] Bouhattate J, Legrand E, Feaugas X. Computational analysis of geometrical factors affecting experimental data extracted from hydrogen permeation tests: I – consequences of trapping. *Int J Hydrogen Energy* 2011;36:12644–52.
- [10] Hurley C, Martin F, Marchetti L, Chêne J, Blanc C, Andrieu E. Numerical modeling of thermal desorption mass spectroscopy (TDS) for the study of hydrogen diffusion and trapping interactions in metals. *Int J Hydrogen Energy* 2015;40:3402–14. <http://dx.doi.org/10.1016/j.ijhydene.2015.01.001>.
- [11] Kim SM, Buyers WJL. Vacancy formation energy in iron by positron annihilation. *J Phys F Met Phys* 1978;8:L103–8. <http://dx.doi.org/10.1088/0305-4608/8/5/001>.
- [12] Song EJ, Suh D-W, Bhadeshia HKDH. Theory for hydrogen desorption in ferritic steel. *Comput Mater Sci* 2013;79:36–44. <http://dx.doi.org/10.1016/j.commatsci.2013.06.008>.
- [13] Fischer FD, Mori G, Svoboda J. Modelling the influence of trapping on hydrogen permeation in metals. *Corros Sci* 2013;76:382–9. <http://dx.doi.org/10.1016/j.corsci.2013.07.010>.
- [14] Legrand E, Feaugas X, Bouhattate J. Generalized model of desorption kinetics: characterization of hydrogen trapping in a homogeneous membrane. *Int J Hydrogen Energy* 2014;39:8374–84. <http://dx.doi.org/10.1016/j.ijhydene.2014.03.191>.
- [15] Legrand E, Oudriss A, Savall C, Bouhattate J. Towards a better understanding of hydrogen measurements obtained by thermal desorption spectroscopy using FEM modeling. *Int J Hydrogen Energy* 2015;40:2871–81. <http://dx.doi.org/10.1016/j.ijhydene.2014.12.069>.
- [16] Olden V, Saai A, Jemblie L, Johnsen R. FE simulation of hydrogen diffusion in duplex stainless steel. *Int J Hydrogen Energy* 2014;39:1156–63. <http://dx.doi.org/10.1016/j.ijhydene.2013.10.101>.
- [17] Zhu J, Chen LQ, Shen J, Tikare V. Microstructure dependence of diffusional transport. *Comput Mater Sci* 2001;20:37–47. [http://dx.doi.org/10.1016/S0927-0256\(00\)00123-3](http://dx.doi.org/10.1016/S0927-0256(00)00123-3).
- [18] Swiler TP, Tikare V, Holm EA. Heterogeneous diffusion effects in polycrystalline microstructures. *Mater Sci Eng* 1997;238:85–93. [http://dx.doi.org/10.1016/S0921-5093\(97\)00441-3](http://dx.doi.org/10.1016/S0921-5093(97)00441-3).
- [19] Lacaille V, Morel C, Feulvach E, Kermouche G, Bergheau JM. Finite element analysis of the grain size effect on diffusion in polycrystalline materials. *Comput Mater Sci* 2014;95:187–91. <http://dx.doi.org/10.1016/j.commatsci.2014.07.026>.
- [20] Legrand E, Bouhattate J, Feaugas X, Touzain S, Garmestani H, Khaleel M, et al. Numerical analysis of the influence of scale effects and microstructure on hydrogen diffusion in polycrystalline aggregates. *Comput Mater Sci* 2013;71:1–9. <http://dx.doi.org/10.1016/j.commatsci.2013.01.018>.
- [21] Jothi S, Croft TN, Wright L, Turnbull A, Brown SGR. Multi-phase modelling of intergranular hydrogen segregation/trapping for hydrogen embrittlement. *Int J Hydrogen Energy* 2015;40:15105–23. <http://dx.doi.org/10.1016/j.ijhydene.2015.08.093>.
- [22] Ilin DN, Kutsenko AA, Tanguy D, Olive J-M. Effect of grain boundary trapping kinetics on diffusion in polycrystalline materials: hydrogen transport in Ni. *Model Simul Mater Sci Eng* 2016;24, 035008. <http://dx.doi.org/10.1088/0956-0393/24/3/035008>.

- [23] Jothi S, Winzer N, Croft TN, Brown SGR. Meso-microstructural computational simulation of the hydrogen permeation test to calculate intergranular, grain boundary and effective diffusivities. *J Alloys Compd* 2015;645:S247–51. <http://dx.doi.org/10.1016/j.jallcom.2014.12.247>.
- [24] Jothi S, Croft TN, Brown SGR. Coupled macroscale-microscale model for hydrogen embrittlement in polycrystalline materials. *Int J Hydrogen Energy* 2015;40:2882–9. <http://dx.doi.org/10.1016/j.ijhydene.2014.12.068>.
- [25] Jothi S, Croft TN, Brown SGR, de Souza Neto EA. Finite element microstructural homogenization techniques and intergranular, intragranular microstructural effects on effective diffusion coefficient of heterogeneous polycrystalline composite media. *Compos Struct* 2014;108:555–64. <http://dx.doi.org/10.1016/j.compstruct.2013.09.026>.
- [26] Dadfarnia M, Martin ML, Nagao A, Sofronis P, Robertson IM. Modeling hydrogen transport by dislocations. *J Mech Phys Solids* 2015;78:511–25. <http://dx.doi.org/10.1016/j.jmps.2015.03.002>.
- [27] Ilin DN, Saintier N, Olive J-M, Abgrall R, Aubert I. Simulation of hydrogen diffusion affected by stress-strain heterogeneity in polycrystalline stainless steel. *Int J Hydrogen Energy* 2014;39:2418–22. <http://dx.doi.org/10.1016/j.ijhydene.2013.11.065>.
- [28] Wu Q, Zikry MA. Prediction of diffusion assisted hydrogen embrittlement failure in high strength martensitic steels. *J Mech Phys Solids* 2015;85:143–59. <http://dx.doi.org/10.1016/j.jmps.2015.08.010>.
- [29] Pouillier E, Gourgues AF, Tanguy D, Busso EP. A study of intergranular fracture in an aluminium alloy due to hydrogen embrittlement. *Int J Plast* 2012;34:139–53. <http://dx.doi.org/10.1016/j.ijplas.2012.01.004>.
- [30] Neeraj T, Srinivasan R, Li J. Hydrogen embrittlement of ferritic steels: observations on deformation microstructure, nanoscale dimples and failure by nanovoiding. *Acta Mater* 2012;60:5160–71. <http://dx.doi.org/10.1016/j.actamat.2012.06.014>.
- [31] Wang S, Martin ML, Sofronis P, Ohnuki S, Hashimoto N, Robertson IM. Hydrogen-induced intergranular failure of iron. *Acta Mater* 2014;69:275–82. <http://dx.doi.org/10.1016/j.actamat.2014.01.060>.
- [32] Li J-X, Oudriss A, Metsue A, Bouhattate J, Feaugas X. Anisotropy of hydrogen diffusion in nickel single crystals: the effects of self-stress and hydrogen concentration on diffusion. *Sci Rep* 2017;7:45041. <http://dx.doi.org/10.1038/srep45041>.
- [33] Brass AM, Chêne J. Influence of deformation on the hydrogen behavior in iron and nickel base alloys: a review of experimental data. *Mater Sci Eng* 1998;242:210–21. [http://dx.doi.org/10.1016/S0921-5093\(97\)00523-6](http://dx.doi.org/10.1016/S0921-5093(97)00523-6).
- [34] Sofronis P, Liang Y, Aravas N. Hydrogen induced shear localization of the plastic flow in metals and alloys. *Eur J Mech - a/Solids* 2001;20:857–72. [http://dx.doi.org/10.1016/S0997-7538\(01\)01179-2](http://dx.doi.org/10.1016/S0997-7538(01)01179-2).
- [35] Xie W, Liu X, Chen W, Zhang H. Hydrogen hardening effect in heavily deformed single crystal  $\alpha$ -Fe. *Comput Mater Sci* 2011. <http://dx.doi.org/10.1016/j.commatsci.2011.06.036>.
- [36] Wang S, Ohnuki S, Hashimoto N, Chiba K. Hydrogen effects on tensile property of pure iron with deformed surface. *Mater Sci Eng* 2013;560:332–8. <http://dx.doi.org/10.1016/j.msea.2012.09.075>.
- [37] Song J, Curtin WA. Mechanisms of hydrogen-enhanced localized plasticity: an atomistic study using  $\alpha$ -Fe as a model system. *Acta Mater* 2014;68:61–9. <http://dx.doi.org/10.1016/j.actamat.2014.01.008>.
- [38] Tien J, Thompson AW, Bernstein IM, Richards RJ. Hydrogen transport by dislocations. *Metall Trans A* 1976;7:821–9.
- [39] Hirth JP. Effects of hydrogen on the properties of iron and steel. *Metall Trans A* 1980;11:861–90. <http://dx.doi.org/10.1007/BF02654700>.
- [40] Taha A, Sofronis P. A micromechanics approach to the study of hydrogen transport and embrittlement. *Eng Fract Mech* 2001;68:803–37. [http://dx.doi.org/10.1016/S0013-7944\(00\)00126-0](http://dx.doi.org/10.1016/S0013-7944(00)00126-0).
- [41] Oriani RA. The diffusion and trapping of hydrogen in steel. *Acta Metall* 1970;18:147–57. [http://dx.doi.org/10.1016/0001-6160\(70\)90078-7](http://dx.doi.org/10.1016/0001-6160(70)90078-7).
- [42] Li JCM, Oriani RA, Darken LS. The thermodynamics of stressed solids. *Zeitschrift Für Physikalische Chemie* 1966;49:271–90. [http://dx.doi.org/10.1524/zpch.1966.49.3\\_5.271](http://dx.doi.org/10.1524/zpch.1966.49.3_5.271).
- [43] Bogkris JO, Beck W, Genshaw MA, Subramanyan PK, Williams FS. The effect of stress on the chemical potential of hydrogen in iron and steel. *Acta Metall* 1971;19:1209–18. [http://dx.doi.org/10.1016/0001-6160\(71\)90054-X](http://dx.doi.org/10.1016/0001-6160(71)90054-X).
- [44] Kumnick AJ, Johnson HH. Deep trapping states for hydrogen in deformed iron. *Acta Metall* 1980;28:33–9. [http://dx.doi.org/10.1016/0001-6160\(80\)90038-3](http://dx.doi.org/10.1016/0001-6160(80)90038-3).
- [45] Simulia. *Abaqus User subroutines reference guide*. Dassault Système 2011;1.1.40–1.1.41.
- [46] Asaro RJ. *Micromechanics of crystals and polycrystals*. *Adv Appl Mech* 1983;23:61–3.
- [47] Peirce D, Asaro RJ, Needleman A. An analysis of nonuniform and localized deformation in ductile single crystals. *Acta Metall* 1982;30:1087–119. [http://dx.doi.org/10.1016/0001-6160\(82\)90005-0](http://dx.doi.org/10.1016/0001-6160(82)90005-0).
- [48] Kysar JW. Addendum to “a user-material subroutine incorporating single crystal plasticity in the ABAQUS finite element program, mech report 178”. Massachusetts: Cambridge; 1991.
- [49] Huang Y. A user-material subroutine incorporating single crystal plasticity in the ABAQUS finite element program, mech report 178. Massachusetts: Cambridge; 1991.
- [50] Lord AE, Besheres DN. Elastic stiffness coefficients of iron from 77° to 673°K. *J Appl Phys* 1965;36:1620–5. <http://dx.doi.org/10.1063/1.1703098>.
- [51] Le LT. *Etude par essais in situ MEB et AFM sur monocristaux des mécanismes de glissement à température ambiante de la ferrite de pureté commerciale*. Université Paris 13, Sorbonne Paris Cité; 2013.
- [52] Franciosi P, Le LT, Monnet G, Kahloun C, Chavanne MH. Investigation of slip system activity in iron at room temperature by SEM and AFM in-situ tensile and compression tests of iron single crystals. *Int J Plast* 2015;65:226–49. <http://dx.doi.org/10.1016/j.ijplas.2014.09.008>.
- [53] Olden V, Thaulow C, Johnsen R, Østby E, Berstad T. Application of hydrogen influenced cohesive laws in the prediction of hydrogen induced stress cracking in 25%Cr duplex stainless steel. *Eng Fract Mech* 2008;75:2333–51. <http://dx.doi.org/10.1016/j.engfracmech.2007.09.003>.
- [54] Moriconi C, Hénaff G, Halm D. Cohesive zone modeling of fatigue crack propagation assisted by gaseous hydrogen in metals. *Int J Fatigue* 2014;68:56–66. <http://dx.doi.org/10.1016/j.ijfatigue.2014.06.007>.
- [55] Oh C-S, Kim YJ, Yoon KB. Coupled analysis of hydrogen transport using ABAQUS. *J Solid Mech Mater Eng* 2010;4:908–17. <http://dx.doi.org/10.1299/jmmp.4.908>.
- [56] Nguyen TH. *Développement d'outils numériques pour la prise en compte du couplage hydrogène-plasticité dans un code éléments finis ; application à l'essai de pliage en U*. Université Paris 13, Sorbonne Paris Cité; 2014.
- [57] Charles Y, Nguyen TH, Gaspérini M. FE simulation of the influence of plastic strain on hydrogen distribution during an U-bend test. *Int J Mech Sci* 2017;120:214–24. <http://dx.doi.org/10.1016/j.ijmecsci.2016.11.017>.

- [58] Quey R, Dawson PR, Barbe F. Large-scale 3D random polycrystals for the finite element method: generation, meshing and remeshing. *Comput Methods Appl Mech Eng* 2011;200:1729–45. <http://dx.doi.org/10.1016/j.cma.2011.01.002>.
- [59] Simulia. Abaqus scripting user's manual. Dassault Système; 2011.
- [60] Salahouelhadj A, Haddadi H. Estimation of the size of the RVE for isotropic copper polycrystals by using elastic–plastic finite element homogenisation. *Comput Mater Sci* 2010;48:447–55. <http://dx.doi.org/10.1016/j.commatsci.2009.12.014>.
- [61] Charles Y, Estevez R, Bréchet Y, Maire E. Modelling the competition between interface debonding and particle fracture using a plastic strain dependent cohesive zone. *Eng Fract Mech* 2010;77:705–18. <http://dx.doi.org/10.1016/j.engfracmech.2009.11.012>.
- [62] Barbe F, Decker L, Jeulin D, Cailletaud G. Intergranular and intragranular behavior of polycrystalline aggregates. Part 1: F.E. model. *Int J Plast* 2001;17:513–36. [http://dx.doi.org/10.1016/S0749-6419\(00\)00061-9](http://dx.doi.org/10.1016/S0749-6419(00)00061-9).
- [63] Diard O, Leclercq S, Rousselier G, Cailletaud G. Evaluation of finite element based analysis of 3D multicrystalline aggregates plasticity: application to crystal plasticity model identification and the study of stress and strain fields near grain boundaries. *Int J Plast* 2005;21:691–722. <http://dx.doi.org/10.1016/j.ijplas.2004.05.017>.
- [64] Ren ZY, Zheng QSA. Quantitative study of minimum sizes of representative volume elements of cubic polycrystals—numerical experiments. *J Mech Phys Solids* 2002;50:881–93. [http://dx.doi.org/10.1016/S0022-5096\(01\)00102-8](http://dx.doi.org/10.1016/S0022-5096(01)00102-8).
- [65] Nygård M, Gudmundson P. Three-dimensional periodic Voronoi grain models and micromechanical FE-simulations of a two-phase steel. *Comput Mater Sci* 2002;24:513–9. [http://dx.doi.org/10.1016/S0927-0256\(02\)00156-8](http://dx.doi.org/10.1016/S0927-0256(02)00156-8).
- [66] Crank J. The mathematics of diffusion. Oxford University Press; 1975.
- [67] Barrer RM. Diffusion in and through solids. Cambridge at the University pres; 1951.
- [68] Fallahmohammadi E, Bolzoni F, Lazzari L. Measurement of lattice and apparent diffusion coefficient of hydrogen in X65 and F22 pipeline steels. *Int J Hydrogen Energy* 2013;38:2531–43. <http://dx.doi.org/10.1016/j.ijhydene.2012.11.059>.
- [69] Komaragiri U, Agnew SR, Gangloff RR, Begley MR. The role of macroscopic hardening and individual length-scales on crack tip stress elevation from phenomenological strain gradient plasticity. *J Mech Phys Solids* 2008;56:3527–40. <http://dx.doi.org/10.1016/j.jmps.2008.08.007>.
- [70] Gangloff RP. Science-based prognosis to manage structural alloy performance in hydrogen. In: Somerdøy B, Sofronis P, Jones R, editors. 2008 International hydrogen conference, Jackson Lake Lodge, Grand teton national park, Wyoming, USA; 2009. p. 1–21.
- [71] Martínez-Pañeda E, Niordson CF, Gangloff RP. Strain gradient plasticity-based modeling of hydrogen environment assisted cracking. *Acta Mater* 2016;117:321–32. <http://dx.doi.org/10.1016/j.actamat.2016.07.022>.
- [72] Martínez-Pañeda E, del Busto S, Niordson CF, Betegón C. Strain gradient plasticity modeling of hydrogen diffusion to the crack tip. *Int J Hydrogen Energy* 2016;41:10265–74. <http://dx.doi.org/10.1016/j.ijhydene.2016.05.014>.